The new MEMS design, Jan-May 2013

National Institute for
subatomic physics

Gravitational group MEMS project

Dave van Wees

Table of Contents

The new MEMS design, Jan – May 2013 1
The old MEMS design (first 'demo' design) 2
Incomplete sacrificial layer etch 2
Sticking to the substrate 2
Insufficient ETA beam performance 4
Etching trenches 7
Insufficient displacement sensing sensitivity 8
The new MEMS design and conceptual designs 11
Structure thickness limitation 12
Improved intermediate mass anchor 13
Improved capacitive sensing model 14
Improved ETA beam performance 20
Prevention of etching errors 24
References 24

The new MEMS design, Jan – May 2013

From January till May 2013 new MEMS designs are developed for etching completion in June by MESA+, part of the UTwente. In this report the new design is presented together with the problems in the old design that caused the design changes.

The old MEMS design (first 'demo' design)

The old design consists of four different versions:

- G1, anti-reverse
- G2, bi-stable
- G3, single guiding spring
- IP, inverted pendulum design (momentary discarded design)

The main weaknesses of the old design discovered during the test phase (Sep – Dec 2012) are:

- Stuck movable device layer structures by incomplete sacrificial layer etch or waste particles in the 2 µm gap between substrate and device layer. Treated in 'SEM Findings' **[1]**.
- Stuck movable device layer structures by sticking onto the substrate because of Van der Waals forces, by for example shocks or dead load. Treated in 'SEM Findings' **[1]**.
- Insufficient ETA beam force range and displacement range for safe 20 µm cantilever spring compression.
- Etching errors for all structures electrically connected to the outer area via the device layer. Treated in 'SEM Findings' **[1]**.
- Insufficient displacement sensing sensitivity due to sensing comb geometry, Brownian noise and non-optimized electronics.

Incomplete sacrificial layer etch

Part of the movable device layer structures were found to be stuck by an incomplete sacrificial layer etch. This occurs when device layer structures are designed thicker than 5 µm. In the old design stuck structures designed to move occur for the ETA beams (6 µm), the intermediate mass anchor (8 µm), the anti-reverse ring structure in the G1 design (8 µm) and possibly the cantilever spring proof mass attachment point (6 ~ 10 µm).

For the ETA beams, intermediate mass anchor and anti-reverse ring it proved practically possible to loosen the stuck structures by exerting a force with a micro-probe. For the proof mass this method didn't succeed. This could be explained by the large proof mass area sticking to the substrate by the hard to control force direction of the micro-probe, in combination with the relatively compliant GAS springs. Another explanation is the extra large sacrificial layer remainder left under the thick proof mass spring attachment structure forming an obstacle for the proof mass to move. Parts of remaining sacrificial layer are also noticed under ETA beam and intermediate mass anchor, but this creates no obstacle for their movement because the remains are smaller and probably also because the relatively high force exerted by the ETA beams.

Sticking to the substrate

A second failure case, sticking to the substrate, is observed for the proof mass, the ETA beams and for the intermediate mass anchor. In this case the sacrificial layer must be etched away completely, creating two opposing flat areas of substrate and device layer. Now the areas could form a Van der Waals bond, for which the bond force is dependent on the surface area and flatness. For thin

structures with relatively small area the bond is disruptable using a probe (observed for ETA beams and intermediate mass anchor). For the large area proof mass this bond turns out to be practically impossible to loosen. The probe is hard to control for out of plane force, easily pushing the proof mass onto the substrate. Return of the mass in movable state is witnessed by chance once, by shocking the MEMS. This risky method has large potential to destroy device layer structures. Loosening the proof mass using a probe also turned out to be unsuccessful. A large force is needed to break the Van der Waals bond and this force turns out to be much higher than the force needed to damage the device layer. Also blowing with a pipet is restricted: the mass will loosen, but will also break off and fly off. Blowing does work for removing contamination, but again only with extreme caution.

The G1 design is very compliant in out of plane direction, compared to the G2 and G3 designs, and has a much larger potential to stick to the substrate. This is because of the 'missing' connection between anti-reverse structure and intermediate mass in the G1 design, now considered a design mistake. This is also the case for the IP design, failing because of the high out-of-plane compliance. The IP MEMS could be possible, but only by using a more complex etch process with out-of-plane stops, not with the SOI process. FEM simulation gives a 3.0 µm proof mass drop due to gravity (z-direction) for the G1 design, see Figure 1. For the G2 design this is 0.42 µm, see Figure 2. The G3 design has a drop of 0.52 µm. Notice the factor 5 scale factor difference between the two figures.

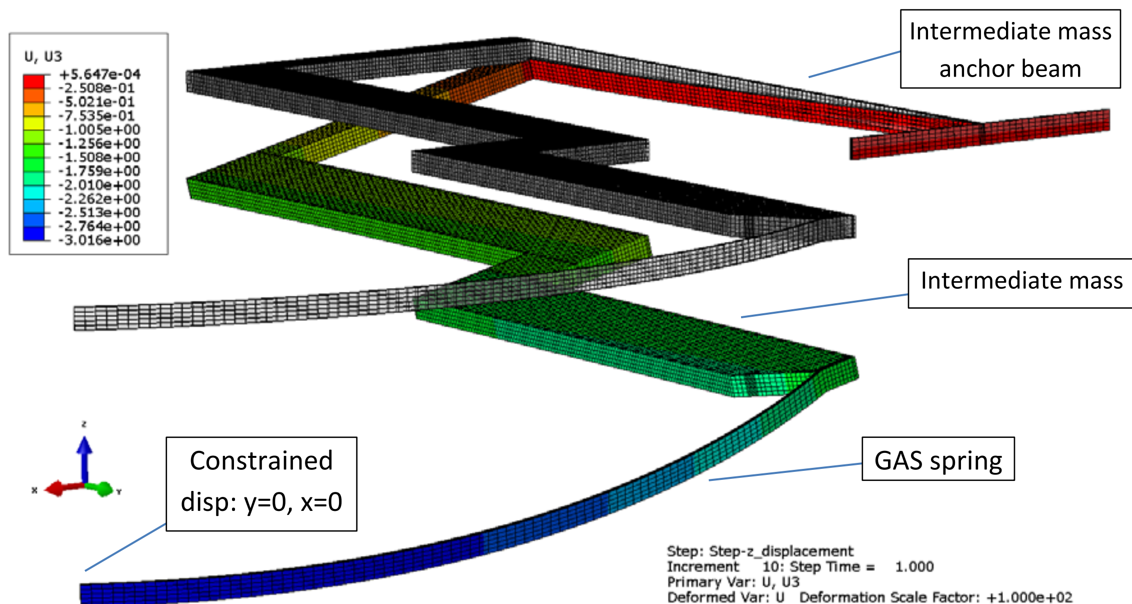

Figure 1: FEM Abaqus G1 anti-reverse intermediate mass simulation. Z-direction displacement under gravity load of 3.0 µm. A point mass of 0.13 mg (quarter of proof mass) is attached to the spring tip. Deformation scale factor = 100.

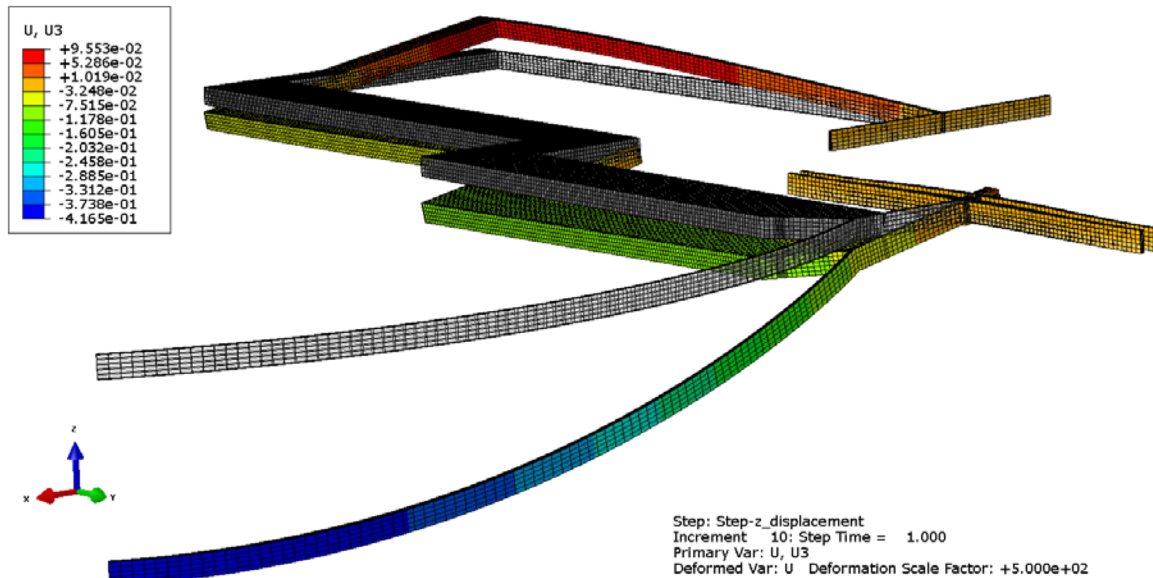

Figure 2: FEM Abaqus G2 bi-stable intermediate mass simulation. Z-direction displacement under gravity load of 0.42 µm. A point mass of 0.13 mg (quarter of proof mass) is attached to the spring tip. Deformation scale factor = 500.

In case of the G1 design the main cause of displacement is torsion of the 1000 µm intermediate mass anchor beam. For the G2 and G3 design the bi-stable beam/guiding spring holds the intermediate mass up, decreasing out of plane compliance. Still the main displacement cause is rotation of the intermediate mass. The long 970 µm cantilever spring magnifies this rotation into a relatively large displacement of the spring tip.

Insufficient ETA beam performance

In the old MEMS design the ETA beams turned out to perform insufficient for realization of the amount of compression in mind (~20 µm). Especially the G2 design, with the hardest to compress bi-stable beam structure, was unable to be compressed more than 10 µm. The bi-stable point is at 12 µm for the old design and at this point the ETA beam is at its very limit. Both bi-stable flipping and breaking of the beam is observed, see Figure 3.

Figure 3: (a) Bi-stable beam successfully flipped by ETA. (b) Bi-stable beam and ETA broken by stress. It is still uncertain if the ETA beam or the bi-stable beam failed first and destroyed the other by impact. It is certain that the ETA beam was at its limit in this case, because it showed melting spots.

The ETA beam behavior is well understood. There is good correspondence of measurements, numerical modeling and FEM modeling. In the models the maximum deflection is limited by the melting temperature of silicon (T = 1600 K). The numerical model uses the electro-thermal model of

Maloney **[2]**, including beam conduction, heat generation and air gap circulation, with added surface radiation. The thermal-mechanical model of Enikov **[3]** is used to calculate the beam tip deflection in unloaded and loaded case.

In Figure 4 the old ETA beam design is shown. All dimensions are given in Table 1 in the next chapter.

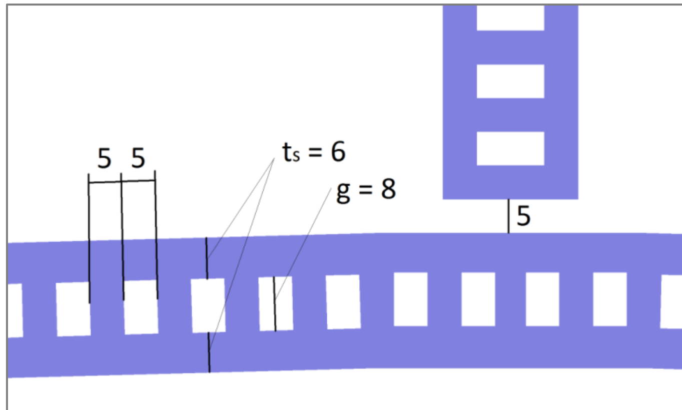

Figure 4: Old ETA beam design outtake with dimensions (units µm). CleWin 5.0 Layout Editor.

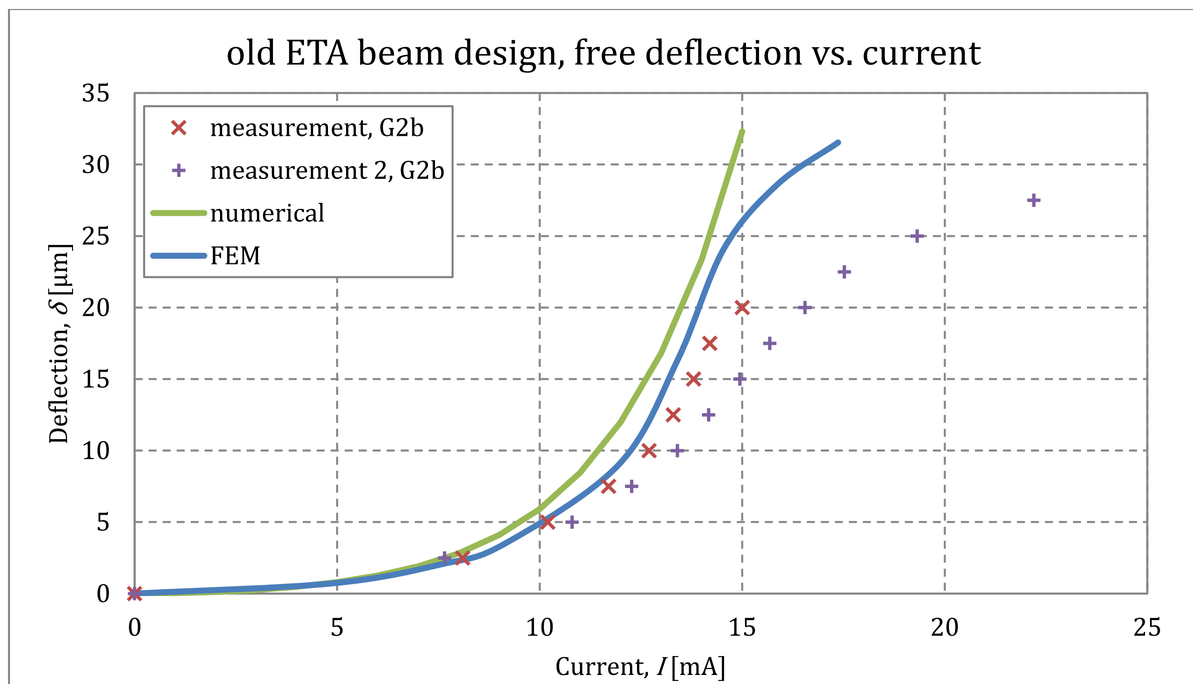

Figure 5: old design ETA beam measured and modeled free tip deflection versus applied current through the beam.

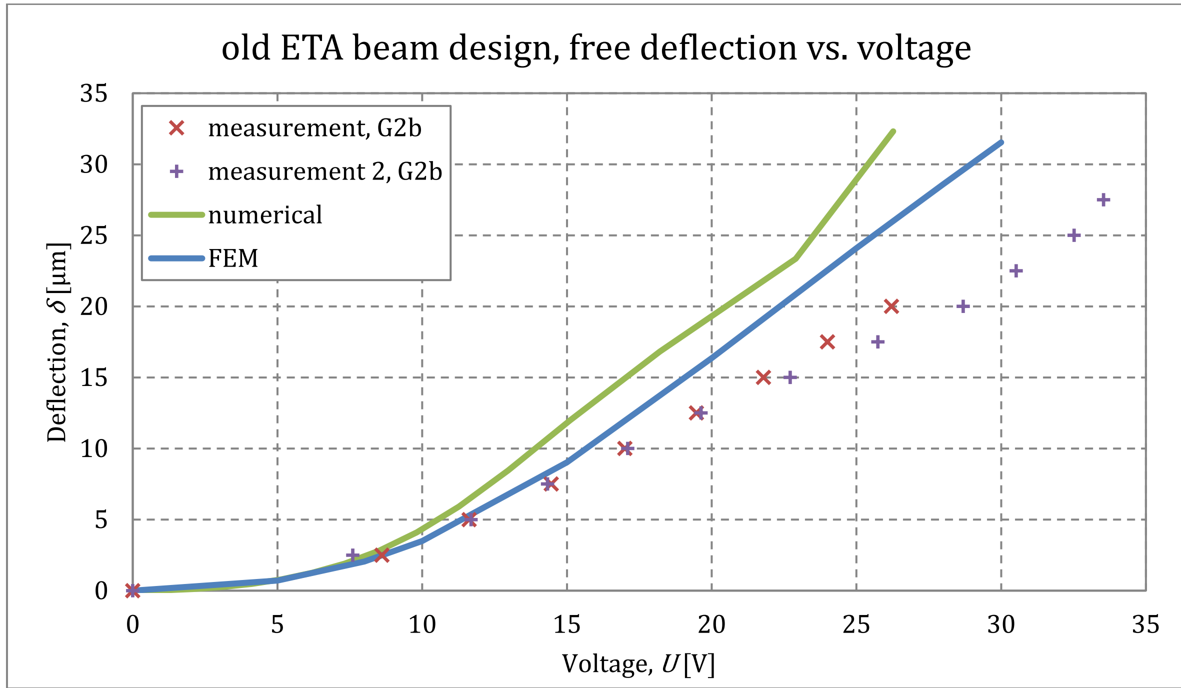

Figure 6: old design ETA beam measured and modeled free tip deflection versus applied voltage over the beam.

Figure 5 and Figure 6 show the results for measurement and modeling of a free deflecting ETA beam. It is seen that the models seem to predict optimistic behavior. The two measurements show large difference even while both measurements are done on the same MEMS, G2b. An explanation could be that two different ETA beams on the chip are measured. Furthermore there is a large time period (several months) between both measurements. In the meantime the mass flew off the chip and possibly the ETA beam is damaged. This is why most certainty should be ascribed to the first measurement.

The resistance measurement analog to the first measurement is used for current to voltage conversion of the numerical model and voltage to current conversion of the FEM model.

Table 1: FEM simulation parameters

Variable	Value at T=293, p=1 bar	formula
Thermal conductivity silicon, k_s	148 [W/mK]	$k_s = 133385 \cdot T^{-1.198}$ (for 294 to 1650 K)
Electrical conductivity silicon, ρ_s	4304 [1/Ωm]	$\rho_s = 0.000764 \cdot T^2 - 2.9669 \cdot T + 5072.3$ (for 293 to 1600 K)
Expansion coefficient, α	2.51 E-6 [1/K]	$\alpha = -2.99 \cdot 10^{-18} \cdot T^4 + 1.36 \cdot 10^{-14} \cdot T^3 - 2.28 \cdot 10^{-11} \cdot T^2 + 1.74 \cdot 10^{-8} \cdot T - 9.11 \cdot 10^{-7}$
Specific heat, c_s	640 [J/kgK]	$c_s = 4.21 \cdot 10^{-7} \cdot T^3 - 0.0014 \cdot T^2 + 1.63 \cdot T + 292.8$
Density, ρ_s	2.32 E3 [kg/m3]	Assumed constant
Young's Modulus	150 GPa	Assumed constant
Poisson's Ratio	0.3	Assumed constant

Etching trenches

SEM imaging revealed etching errors in device layer walls, with possible effect on the mechanical properties of the mechanical structures in this layer. These errors were named ‘Etching trenches’ **[1]**. Extensive observation of all possible walls formed the conclusion that the trenches occur in all structures connected (e.g. electrically connected) to the outer area of the device layer. This is caused by the deep-reactive ion (DRIE) etching process in which a potential is applied on the wafer for accelerating the etch ions. In the G1 design all structures are isolated from the outer area by chance and all structures except the outer edge are intact. In the G2 and G3 design almost all structures are connected to the outer area and thus damaged. This is explained in more detail in the report ‘SEM Findings 23-01-2013’ **[1]**.

Insufficient displacement sensing sensitivity

For application of MEMS accelerometers for Newtonian Noise subtraction for the Einstein Telescope (ET) a sensor with 1 ng/rtHz of self-noise in the low frequency regime (1 – 10 Hz) is needed. The best known MEMS sensitivity reached is 10 ng/rtHz at 200 Hz for the best HP sensor **[4]**.

The 32kHz excitation signal on the sensing comb bridge results in a current source

$$I_{sensor} = j\omega\Delta C V_e$$

where in practical case the bridge excitation frequency $\omega = 2\pi \cdot 32\ \mathrm{kHz}$, the sensing capacitance C_s changes with $\Delta C = 0.06\ \mathrm{pF}/\mu\mathrm{m}$ and the bridge excitation voltage amplitude is adjustable from $V_e = 10\ \mathrm{mV}$ up to $3.9\ \mathrm{V}$. This gives an estimate value for 1 μm displacement of $I_{sensor} = 0.12\ \mathrm{nA}$ up to $I_{sensor} = 47\ \mathrm{nA}$.

This current enters the preamp, type OpAmp AD 797, giving the output voltage:

$$V_{out} = -\frac{\Delta C V_e}{C_f + \dfrac{C_s + C_f + C_p + C_{inp}}{A}}$$

where C_f is the feedback capacitor, C_p is the parasitic capacitance, C_{inp} is the OpAmp input capacitance and A is the preamp open loop gain, which is $A \gg 1$ in case of relative high excitation frequency combined with a high feedback resistance R_f. Then the equation reduces to

$$V_{out} = -V_e \frac{\Delta C}{C_f}$$

The practical case of 1 μm displacement and $C_f = 2.2\ \mathrm{pF}$ gives $V_{out} = 0.27\ \mathrm{mV}$ for $V_e = 10\ \mathrm{mV}$ and $V_{out} = 0.11\ \mathrm{V}$ for $V_e = 3.9\ \mathrm{V}$.

The preamp output noise is the quadrature sum of:

- Johnson noise of R_f, shunted by C_f

$$\frac{1}{\omega R_f C_f}\sqrt{4k_B T R_f} = \frac{1}{2\pi \cdot 32k \cdot 4.7M \cdot 2.2p}\sqrt{4 \cdot 1.38 \cdot 10^{-23} \cdot 293 \cdot 4.7M} = 0.13\ \mu\mathrm{V}/\sqrt{\mathrm{Hz}}$$

- The OpAmp has an input current noise $i_{ein} = 0.1\ \mathrm{fA}/\sqrt{\mathrm{Hz}}$ and voltage noise $v_{ein} = 3\ \mathrm{nV}/\sqrt{\mathrm{Hz}}$. The input current noise appears at the output as a voltage:

$$\frac{i_{ein}}{\omega C_f} = 0.23\ \mathrm{nV}/\sqrt{\mathrm{Hz}}$$

where $C_f = 2.2\ \mathrm{pF}$ is the feedback capacitor.

- And the input voltage noise appears at the output as (in case of $A \gg 1$):

$$v_{ein}\frac{C_s + C_f + C_p + C_{inp}}{C_f} = 3\left[\frac{\mathrm{nV}}{\sqrt{\mathrm{Hz}}}\right]\frac{0.21 + 2.2 + 300 + ???\ [\mathrm{pF}]}{2.2\ [\mathrm{pF}]} = 0.41\ \mu\mathrm{V}/\sqrt{\mathrm{Hz}}$$

The total preamp output noise is the quadrature sum of all three previous noise types:

$$\sqrt{(0.13\mu)^2 + (0.23\text{n})^2 + (0.41\mu)^2} = 0.43\ \mu\text{V}/\sqrt{\text{Hz}}$$

and thus is dominated by the parasitic capacitance.

The Brownian noise at DC (1 Hz) and atmospheric pressure ($P = 10^5$ Pa) is given by

$$a_{tn}(\omega, P) = \sqrt{\frac{4k_BT}{m}\left(\frac{D(P)}{m} + \frac{\phi\omega_u^2}{\omega}\right)} = \sqrt{\frac{4 \cdot 1.38 \cdot 10^{-23} \cdot 293}{0.5 \cdot 10^{-6}}\left(\frac{1.4 \cdot 10^{-4}}{0.5 \cdot 10^{-6}} + \frac{10^{-5} \cdot (2\pi \cdot 240)^2}{2\pi \cdot 1}\right)}$$
$$= 3\frac{\frac{\mu\text{m}}{s^2}}{\sqrt{\text{Hz}}} = 300\ \text{ng}/\sqrt{\text{Hz}}$$

For the old MEMS design the noise level is -114 (+20dB by probe) = -94 dB, which corresponds to 13 µg/√Hz. By enlarging the sensing amplifier resistor (R4) from 47kΩ to 4,7 MΩ (factor 100) and setting R133 from x10 to x1 (to avoid clipping), the noise level drops to -120 (+20 dB by probe) = -100 dB, which corresponds to 7 µg/√Hz.

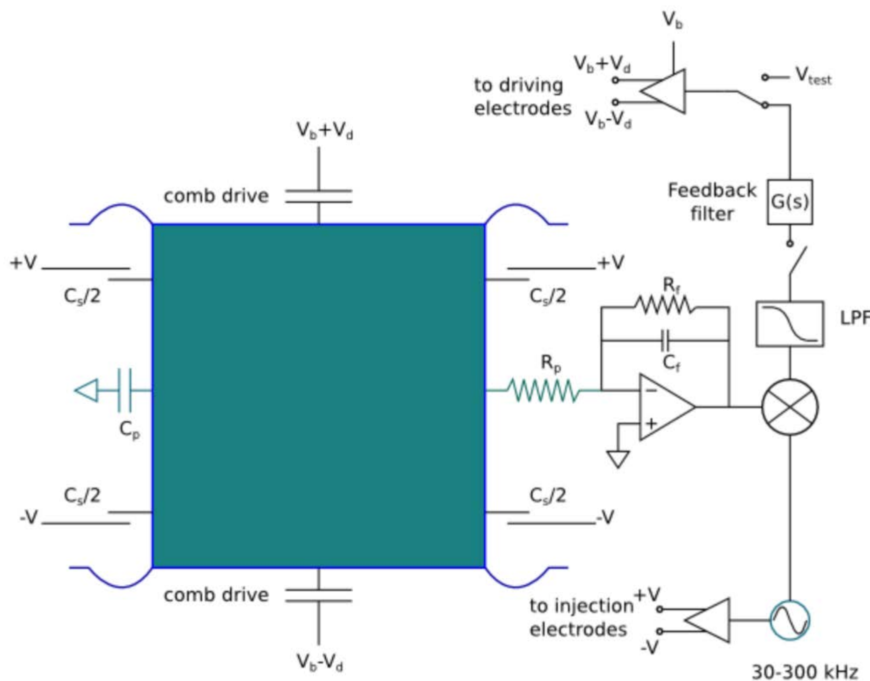

Figure 7: Schematic electronic circuit sensing combs.

Appendix:

The noise level in dB is calculated to g/√Hz as follows (example for -114 dB):

Factor 10 weakening by probe gives -94 dB/rtHz.

$$SNR = -94\ \text{dB}/\sqrt{\text{Hz}} = 20\log\frac{x}{1\ [\text{V}]}$$

$$x = 1\ [V] \cdot 10^{\frac{-94}{20}} = 20\ \mathrm{\mu V}/\sqrt{\mathrm{Hz}}$$

Sensing combs calibration: ~1.5 V/g

$$noise = \frac{20\ [\mathrm{\mu V}/\sqrt{\mathrm{Hz}}]}{1.5\ [\mathrm{V/g}]} = 13\ \mathrm{\mu g}/\sqrt{\mathrm{Hz}}$$

The new MEMS design and conceptual designs

The new design consist of five different versions:

- G1.2, improved anti-reverse
- G2.2, improved bi-stable
- G3.2, improved single guiding spring
- G4.2, conceptual design without intermediate mass and smaller sensing gaps
- G5.2, conceptual design without intermediate mass and vertical sensing fingers

The main universal improvements in respect to the old design are:

- Allowing only ≤5 µm movable structure thickness. All thicker structures are slimmed or removed.
- Improved intermediate mass anchor, reducing compliance of the proof mass in out of plane direction and thus counteracting sticking to the substrate. Also the y-direction stiffness is increased, reducing intermediate mass rotation and unequal compression.
- Increased ETA beam force and displacement range by geometry optimization and heat sinks. Also the ETA beams are doubled as backup for large force applications.
- Elimination of etching trenches by isolation from the outer device layer area.

Less important add-ons are:

- Measuring gauges for displacement measurement of spring compression and proof mass displacement.
- MEMS type id etched in outer device layer area.

Design version specific changes are:

- G1.2: solid connection between anti-reverse structure and intermediate mass, reducing out of plane compliance. Also the anti-reverse part and probe ring are swapped for the same reason.
- G1.2: extra anti-reverse ratchet holes for the possibility to lock large compressions up to 50 µm in steps of 10 µm.
- G2.2 and G3.2: increased separation between the bi-stable springs and guiding springs for reduction of in plane rotation when compressing the cantilever springs.
- G4.2 and G5.2: intermediate mass removed for simplification of the design and extra space for possible new sensing structures. Calculations show that the out of plane compliance of the G2 and G3 designs is low enough to try this simplification.
- G4.2: reduced sensing comb gap for higher sensing signal and overall signal-to-noise ratio.
- G5.2: Vertical sensing comb fingers for a larger y-direction displacement range of the proof mass and a directly linear sensing signal. For this change the proof mass is reduced in width to create space for the large amount of fingers needed in this configuration to maintain sensitivity. Also the proof mass is lengthened to maintain the same weight.
- G4.2 and G5.2: added test structures in the outer area of the device layer. Free ETA beam with gauge, ETA beam with force measuring beam, ETA beam with anti-reverse force measurement and thermal displacement read-out test.

Structure thickness limitation

All movable structures are reduced to the ≤5 µm thickness needed to improve sacrificial layer etch quality and consistency. Below a summary of all changed structures because of the structure thickness criteria is given.

- ETA beams, 6 µm
- Intermediate structure pushing tips, max 13 µm
- Probe ring, 8 µm
- Proof mass spring attachment points, 9 µm
- Intermediate mass anchor, 8 µm

For all these structures sacrificial layer remains are observed, as shown for an intermediate mass anchor in Figure 7 and for an ETA beam in Figure 8.

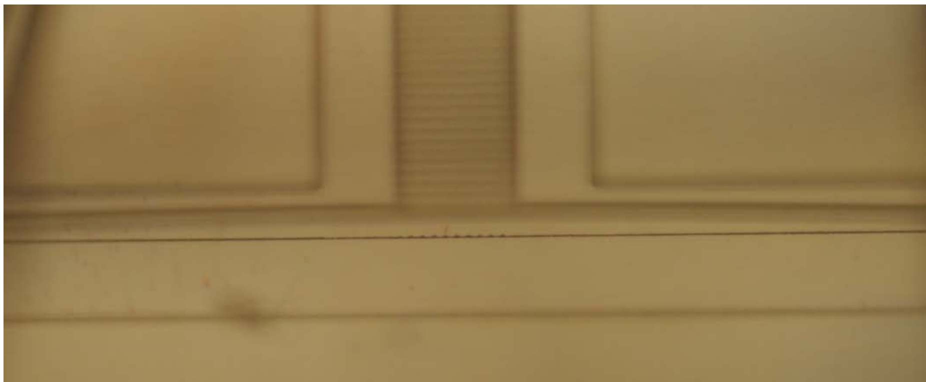

Figure 8: Intermediate mass anchor remains of sacrificial layer, structure thickness of 8 µm. focused on substrate, 200x magnification.

Figure 9: Dotted sacrificial layer remains below a destroyed ETA beam, with structure thickness of 6 µm. Also four spots are shown at the place of the fillets of a bi-stable beam structure. Focused on substrate, 200x magnification.

For structures not much thicker than the 5 µm design limit (for example the ETA beams, 6 µm), sacrificial layer remains aren't always present, dependent on the duration of the HF vapor etching process. This process varies in … µm per minute [].

Reducing structure thickness to maximal 5 µm decreases stiffness, demanding important design changes for ETA beams and intermediate mass anchor. The new intermediate mass anchor design is discussed in the next chapter. The new ETA beam design is discussed onwards.

Improved intermediate mass anchor

The 5 μm design limit demands a new intermediate mass anchor design. The anchor is made as stiff as possible in out of plane direction and y-direction while maintaining large compliance in the compression direction (x-direction). In case of a 5 μm intermediate mass anchor beam in a G1 anti-reverse design with connected spring and anti-reverse structure, the proof mass would drop 0.64 μm in case of a 1 g load and 1.27 μm in case of 2 g. The relation of load and z-displacement is linear for small displacement (only displacements <2 μm taken into account). For the G2 design the z-displacement is 0.45 μm for 1 g in case of this 5 μm beam. For the G3 design this is 0.58 μm. All values are summarized in Table 1.

Table 2: Proof mass z-displacement for 1 g load. (*For the 8 μm anchor there is no connection between GAS spring and anti-reverse structure, corresponding to the old G1 design. For the 5 μm anchor there is a connection, representing a G1.2 design without added second anchor)

	Old (8 μm anchor)	Old (5 μm anchor)	New
G1(.2)	3.0 *	0.64 *	0.39
G2(.2)	0.42	0.45	0.19
G3(.2)	0.52	0.58	0.22

As stiffening measure a second anchor is added in the new G1.2, G2.2 and G3.2 designs. This anchor reduces the dominant torsion of the long anchor beam. This structure forms a H-shaped spring. Furthermore H-shaped springs are added at the ends of each anchor. This secondary H-shaped spring reduces torsion of the short end suspension beams while maintaining compliance for compression. In Figure 9 the new structure is shown.

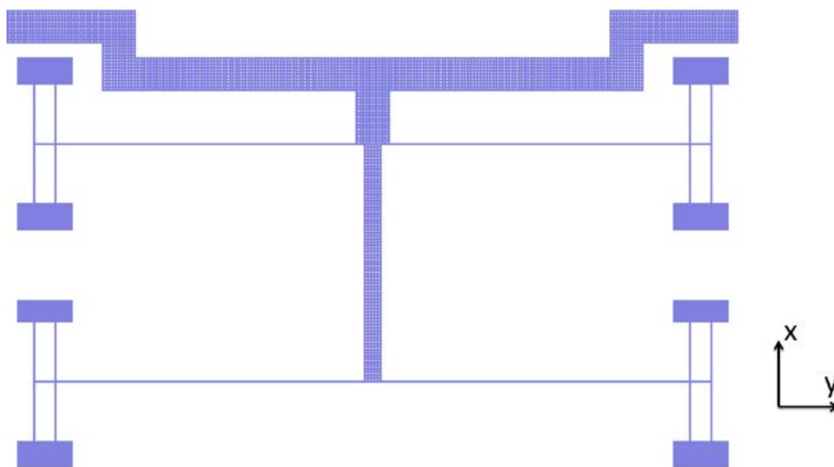

Figure 10: Intermediate mass anchor H-spring structure. CleWin 5.0 Layout Editor.

The intermediate mass anchor has an x spring constant of 1.7 N/m initially up to 2.4 N/m at 30 μm compression. The z spring constant is 33.1 N/m and the y spring constant is 66.7 N/m. For comparison the old anchor design has an almost constant x spring constant of 3.1 N/m, the z spring constant is 11.7 N/m and the y spring constant is 4 N/m. The new anchor performs better in all three DOF's: at average a factor 1.5 weaker in x-direction, a factor 3 stiffer in z-direction and a factor 17 stiffer in y-direction. These values are summarized in Table 2.

Table 3: Intermediate mass stiffness for old design and new design with added second anchor and secondary H-shaped springs.

	Old stiffness	New stiffness	Factor
x	3.1	1.7 – 2.4	0.55 – 0.77
y	4	66.7	16.7
z	11.7	33.1	2.8

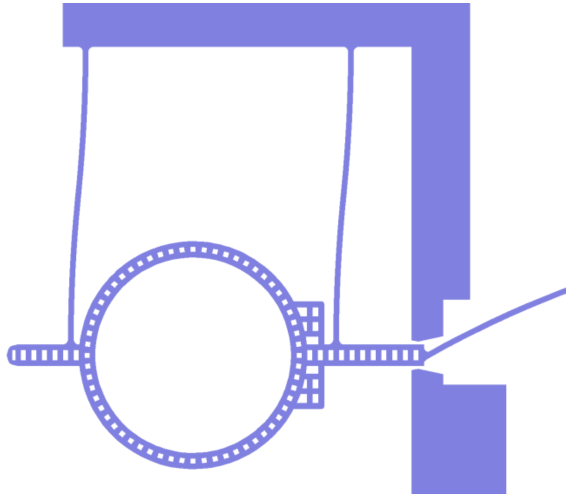

Figure 11: G4.2 spaced guiding springs to compensate for no intermediate mass. CleWin 5.0 Layout Editor.

The two conceptual designs, G4.2 and G5.2, are based on the idea of simplicity and improved sensing output. The total intermediate mass structure is removed, creating space for a potential more complex sensing structure and test structures in the outer border of the 9x9 mm design area. The G3 guiding springs are used for compression guidance. The G3 is best for test purposes because the compression can be returned while maintaining out-of-plane stability. The guiding springs are spaced to keep the guidance in plane and aligned, see Figure 11. This spaced version is also combined with the intermediate mass in the G2.2 and G3.2 designs for an even more rigid suspension. In the G4.2 design the sensing finger gaps are reduced to d_1 = 6 µm and d_2 = 18 µm, pared with place for more fingers (30 to 44 fingers) increasing the sensitivity by a factor 4.1 compared to d_1 = 10 µm and d_2 = 30 µm used in the first design.

Improved capacitive sensing model

The capacitance of one comb (1 quadrant of total) is given by

$$C_{comb} = \left(\frac{\varepsilon_0 hL}{d_1 + y} + \frac{\varepsilon_0 hL}{d_2 - y}\right) C_c N \,, \tag{1}$$

where ε_0 is the vacuum permittivity constant, h is the device layer height, L is the finger overlap, d_1 is the small gap distance, d_2 is the big gap distance and y is the proof mass displacement in the working direction. Multiplied by N, the number of finger pairs per comb. The capacitance geometry factor C_c corrects for the geometry with respect to the ideal parallel plate model. The factor considers fringing fields, comb finger end effects and the substrate laying 2 µm below the comb. Non-dimensionalization of the capacitance gives a generalized analytical form:

$$C^* = \frac{C_{comb}}{C_0} = \frac{1}{1+y^*} + \frac{1}{f-y^*}, \tag{2}$$

And

$$C_0 = \frac{\varepsilon_0 hLNC_c}{d_1}, \tag{3}$$

where $y^* = y/d_1$ is the non-dimensional proof mass displacement and $f = d_2/d_1$ is the ratio between the big gap and small gap. In Figure 11, C^* is plotted for different values of f. Analogous the absolute non-dimensional sensitivity of one comb is given by

$$\frac{dC^*}{dy^*} = \frac{1}{(1+y^*)^2} - \frac{1}{(f-y^*)^2}, \tag{4}$$

The result is plotted in Figure 13 for different values of f.

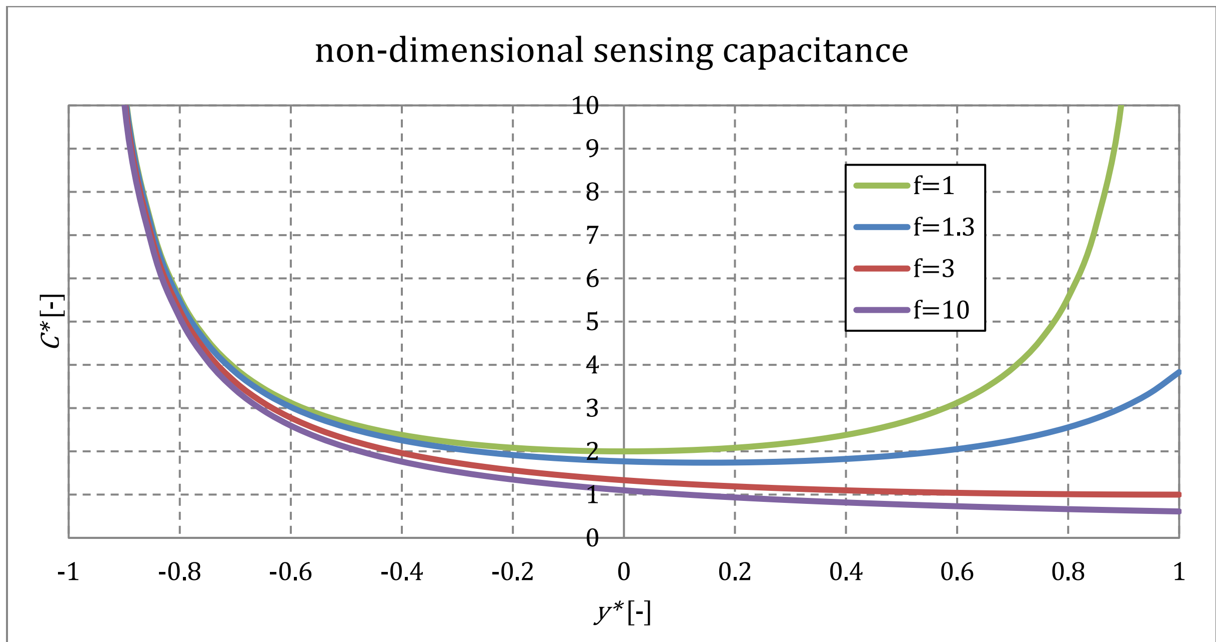

Figure 12: Non-dimensional one comb sensing capacitance for different values of gap ratio f=d_2/d_1.

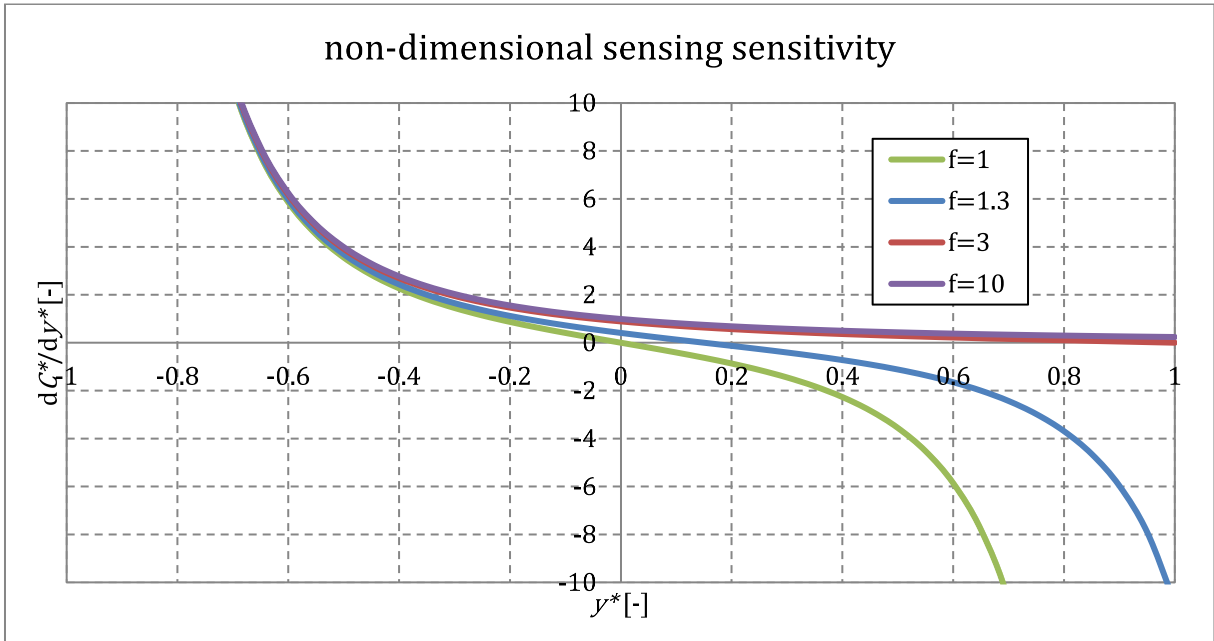

Figure 13: Non-dimensional one comb sensing sensitivity for different values of gap ratio f=d_2/d_1.

All first/old version MEMS designs and the new G1.2, G2.2 and G3.2 designs have identical sensing comb geometry. A 10 µm small gap is combined with a 30 µm big gap. This relatively large gap distance gives the possibility for large proof mass displacements in y-direction, up to 8 µm, which is preferable over sensing sensitivity in the MEMS test phase. On the contrary, the new conceptual G4.2 design has a 6 µm small gap and a 18 µm big gap which restricts proof mass movement to 5 µm and increases sensing sensitivity by a factor 10/6 per finger. In Figure 13 and Figure 14 the one comb capacitance and sensitivity is given respectively in case of d_1= 10 µm and d_1= 6 µm with f= 3. In both cases values are h= 25 µm, L= 237 µm and C_c= ???. The number of fingers, N, is given by

$$N = \frac{l}{g} = \frac{l}{d_1 + d_2 + 2t}, \tag{5}$$

where l= 1492 µm is the proof mass length, g is the length of a unit cell (finger pair) and t= 5 µm is the finger thickness.

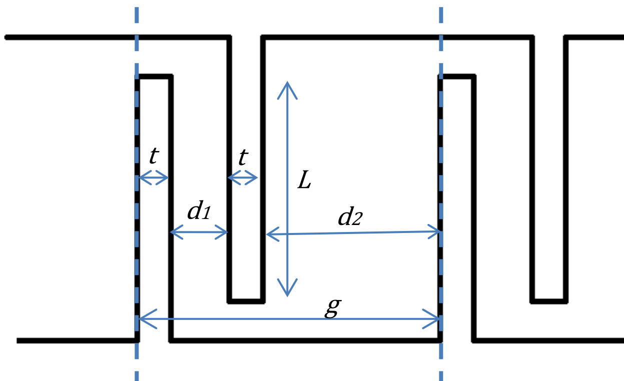

Figure 14: sensing fingers schematic, unit cell indicated by dashed lines.

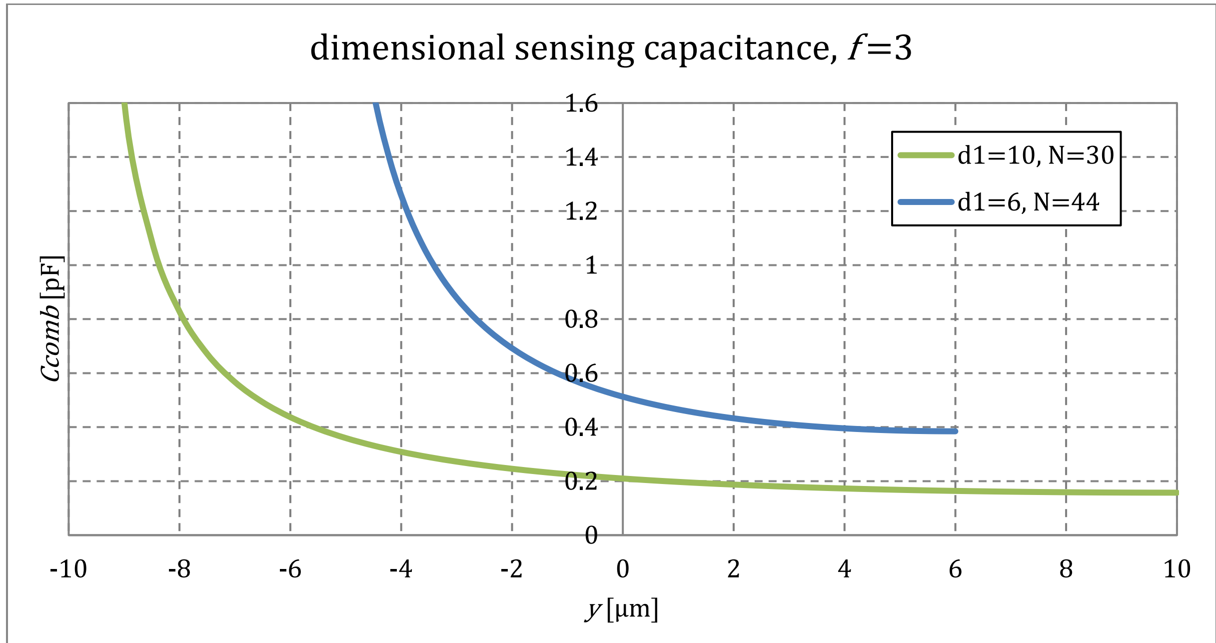

Figure 15: One comb sensing capacitanced_1= 10 µm versus d_1= 6 µm. The gap distance of 6 is used in the G4.2 MEMS design.

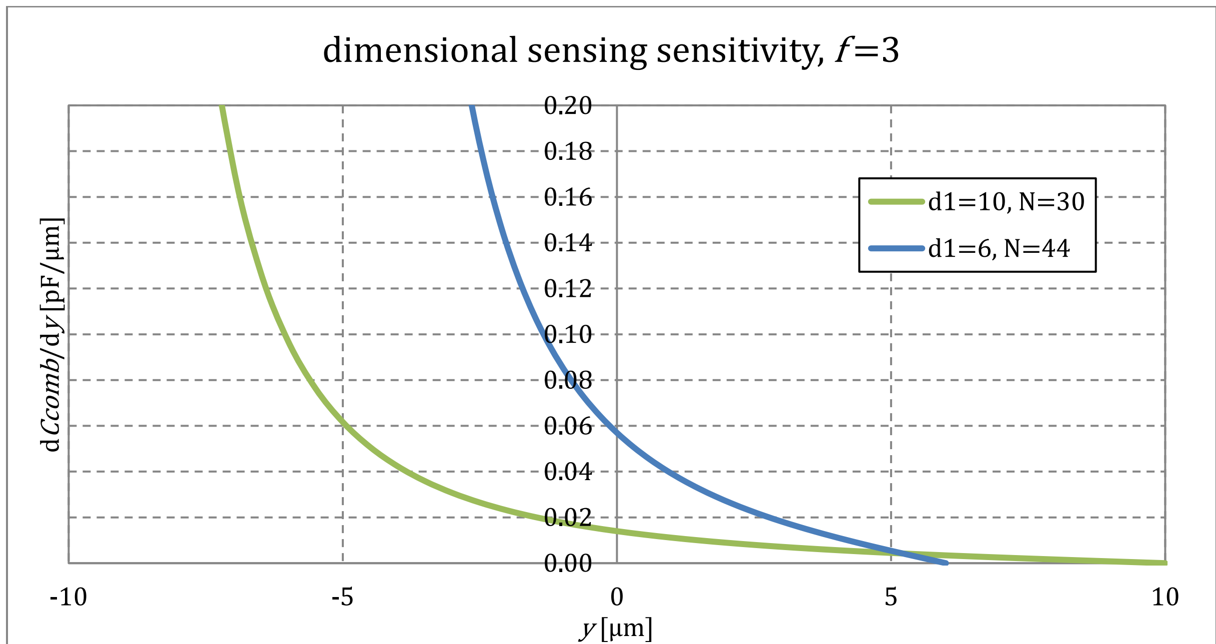

Figure 16: One comb sensing sensitivity d_1= 10 µm versus d_1= 6 µm. The gap distance of 6 is used in the G4.2 MEMS design.

The capacitance per comb when the proof mass is centered is 0.21 pF and 0.51 pF in case of d_1= 10 µm and d_1= 6 µm respectively. The corresponding sensitivity is 0.014 pF/µm and 0.057 pF/µm respectively.

The total sensing capacitance is given by

$$C_{total}(y) = 2C_{comb}(y) + 2C_{comb}(-y)\,, \tag{6}$$

resulting in Figure 15.

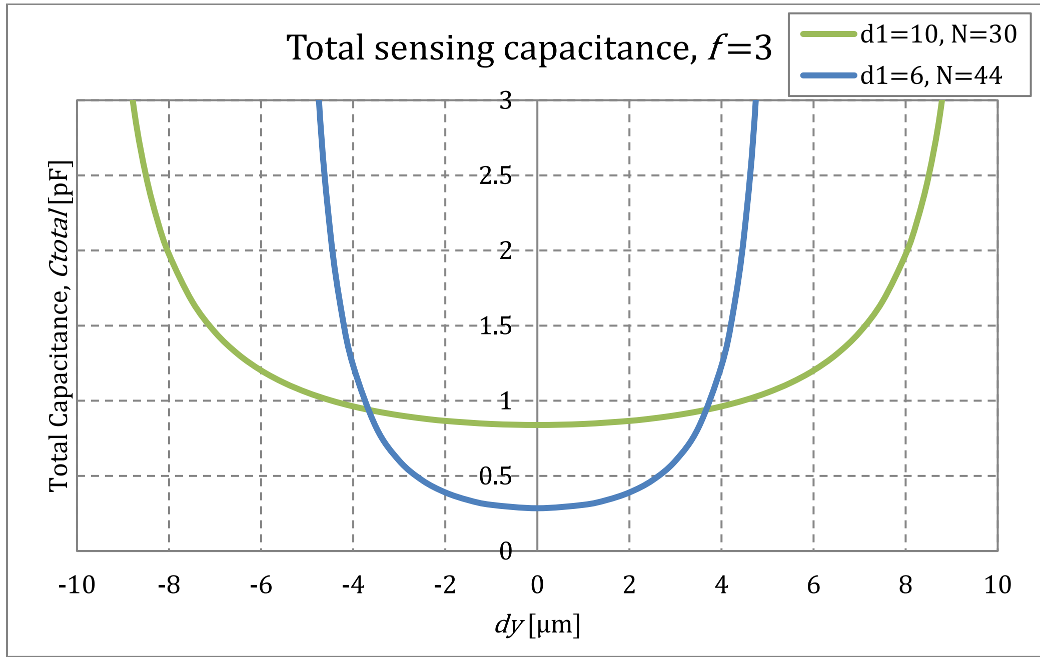

Figure 17: Total sensing capacitance for d_1= 10 µm and d_1= 6 µm.

For small displacement the total capacitance is about constant. The relation of capacitance versus displacement becomes highly non-linear when the small gap distance approaches zero.

The total sensitivity can be summed in different ways, dependent on sensing of linear displacement or rotation of the proof mass. In case of displacement sensing:

$$\left(\frac{dC_{total}}{dy}\right)_y = \left(\frac{dC}{dy}_{comb1} - \frac{dC}{dy}_{comb2}\right) + \left(\frac{dC}{dy}_{comb4} - \frac{dC}{dy}_{comb3}\right) \\ = 2\frac{dC}{dy}_{comb}(y) + 2\frac{dC}{dy}_{comb}(-y)\,, \tag{7}$$

and in case of rotation sensing:

$$\left(\frac{dC_{total}}{dy}\right)_\varphi = \left(\frac{dC}{dy}_{comb1} - \frac{dC}{dy}_{comb3}\right) + \left(\frac{dC}{dy}_{comb2} - \frac{dC}{dy}_{comb4}\right), \tag{8}$$

where $C_{comb\ 1-4}$ are the comb quadrants numbered in circular way. The total sensitivity in case of linear displacement is shown in Figure 16.

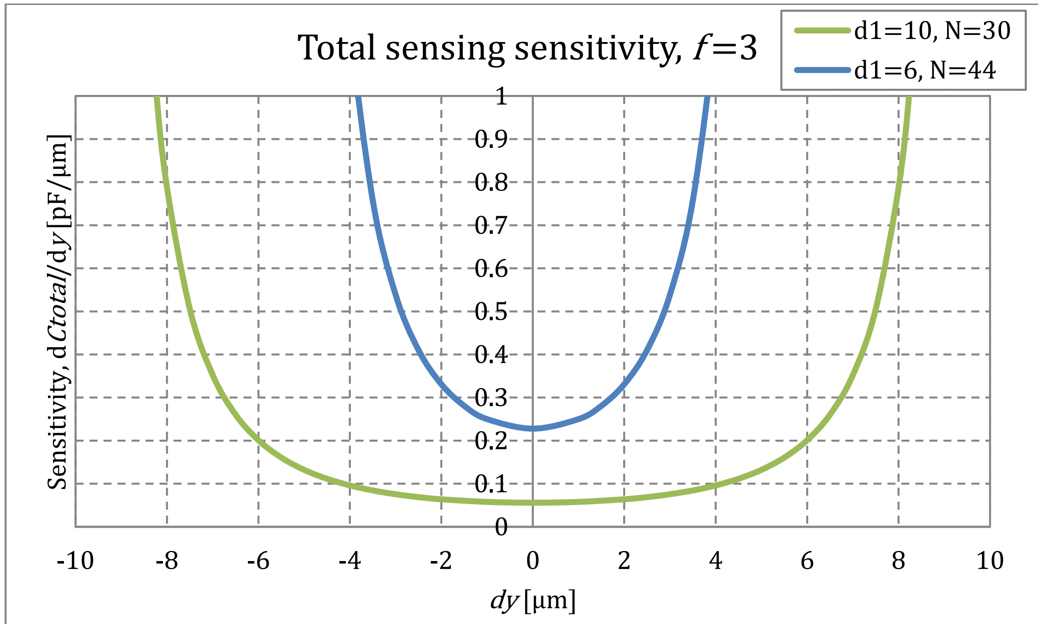

Figure 18: Total sensing linear sensitivity for d_1= 10 µm and d_1= 6 µm.

The total sensitivity around the center is 0.06 pF/µm and 0.23 pF/µm in case of d_1= 10 µm and d_1= 6 µm respectively, see Table 4. There is a factor 4.1 sensitivity increase for the G4.2 conceptual design. The relation of sensitivity versus displacement is non-linear. For d_1= 10 µm an almost constant sensitivity is present for displacements up to 5 micron, the geometry with d_1= 6 µm is only constant for about 1 µm.

The G5.2 conceptual design uses vertical sensing comb fingers for capacitive sensing with large displacement range of the proof mass up to 24 µm. Another advantage is that the vertical comb sensitivity is constant over displacement apart from non-ideal plate capacitor effects. The capacitance and sensitivity is approximated by an ideal parallel plate capacitor. For the G5.2 design, a finger length of L= 40 µm, device layer height h= 25 µm, finger distance d= 10 µm, and amount of finger pairs N= 224, gives a total capacitance of 0.20 pF and a sensitivity of 0.005 pF/µm, see Table 4.

Table 4: Analytical calculated capacitance and sensitivity for all different geometries.

	Horizontal d_1= 10	Horizontal d_1= 6	Vertical d= 10 µm
Total capacitance [pF]	0.84	0.28	0.20
Total sensitivity [pF/µm]	0.06	0.23	0.005

The sensitivity can also be improved by optimization of the electronics. The sensor output, including electronics board circuit, is estimated, using electronics simulation software, to be 820 mV per 1 pF capacitance change per 1 V (amplitude of sine wave) of excitation on each pair of sensing combs. In this case the second AC amplifier stage has a gain of 10 in a range from 1 to 10. In this same simulation the output noise is estimated to be about 10 µV/√Hz. This is noise is independent on the AC excitation voltage. The sensor output signal could be enlarged by a factor 10 by changing the feedback resistor of 47kΩ to 47MΩ, improving sensor output to 11 V per 1 pF capacitance change. Then the noise grows to 40 µV/√Hz, improving the signal-to-noise ratio by a factor 3.

Improved ETA beam performance

The new Electro-thermal actuator design is based on the same working principle as the first version. The beam with initial V-shape expands by Joule heating and deflects, exerting a force on the cantilever spring to be compressed. The ETA beam design is improved by geometry optimization for maximal deflection and force. Also a second beam copy is added to double the force range of the actuator.

In order to get insight in the optimal ETA geometry a simplified analytical model is used in which only thermal strain and stretching strain are considered. Bending strain is neglected. The maximal force the ETA beam can deliver is calculated by the sum of the thermal strain and the counteracting stretching strain:

$$F_{work} = (\varepsilon_T - \varepsilon)EA\sin\theta \tag{9}$$

Where the thermal strain is approximated by:

$$\varepsilon_T = \bar{\alpha}\Delta\bar{T} \tag{10}$$

And the stretching strain is given by:

$$\varepsilon = \frac{\Delta L}{L}$$

The stretching strain, ε, is derived from the geometry change as sketched in Figure 17.

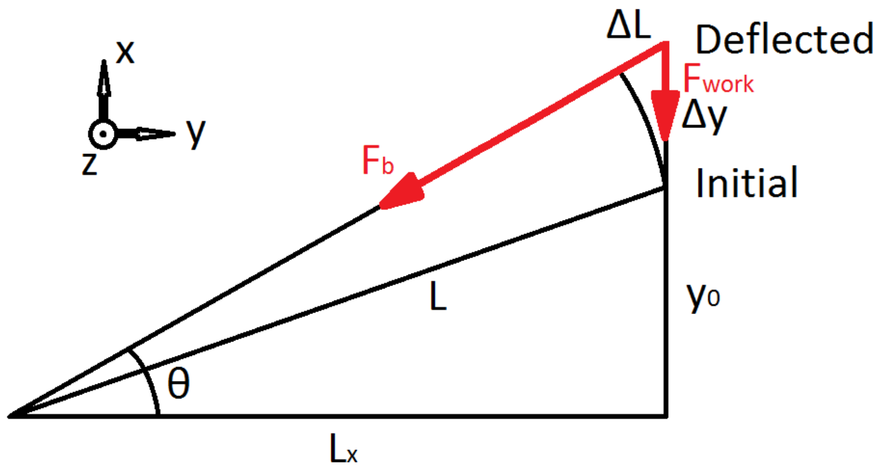

Figure 19: ETA beam simplified model sketch.

Pythagoras' theorem gives, using $\Delta L = \varepsilon L$:

$$\begin{gathered} {y_0}^2 + {L_x}^2 = L^2 \\ \underline{(y_0 + \Delta y)^2 + {L_x}^2 = L^2(1+\varepsilon)^2 \quad -} \\ \Delta y(2y_0 + \Delta y) = \varepsilon L^2(2+\varepsilon) \end{gathered} \tag{11}$$

Solving for ε gives:

$$\varepsilon = \frac{-L + \sqrt{L^2 + dy^2 + 2dyy_0}}{L} = \sqrt{1 + \left(\frac{dy}{L}\right)^2 + \frac{2dyy_0}{L^2}} - 1 \tag{12}$$

Furthermore Figure 17 shows that $\sin\theta$ can be written as:

$$\sin\theta = \frac{y_0 + \Delta y}{L(1+\varepsilon)} \tag{13}$$

The maximal force F_{work} is limited by the buckling force of the beam, see the red force arrows in Figure 17. The beam is able to buckle in the second order in plane mode and in the first order out of plane mode (z-direction). The latter turns out to be the maximal work limiting factor, because of the factor 2 lower buckling force. The out of plane buckling force is given by:

$$F_{b,x} = \frac{4\pi^2 E I_x}{L^2} \tag{14}$$

The x-direction component of this buckling force is given by:

$$F_{max} = F_b \sin\theta \tag{15}$$

In Figure 18 The analytical results are plotted for the old and new ETA beam design. Furthermore FEM Abaqus simulation results are plotted. Design geometry parameters are given in Table 1.

Table 5: ETA beam design geometry parameters.

	Old design	New design
L [µm]	1462	1680
θ0 [°]	1,53	1,53
y0 [µm]	18,99	21,90
ts [µm]	6	5
tm [µm]	0	5
g [µm]	8	3,5
r [µm]	7	8,5
b [µm]	14	22
p [-]	73	6
Ix [µm^4]	15625	19531
Iz [µm^4]	15600	18844

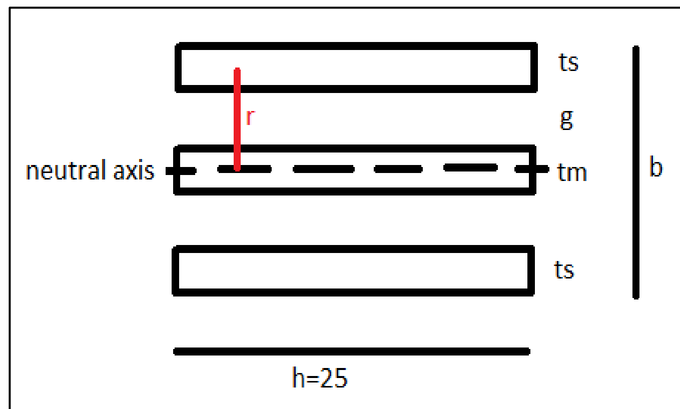

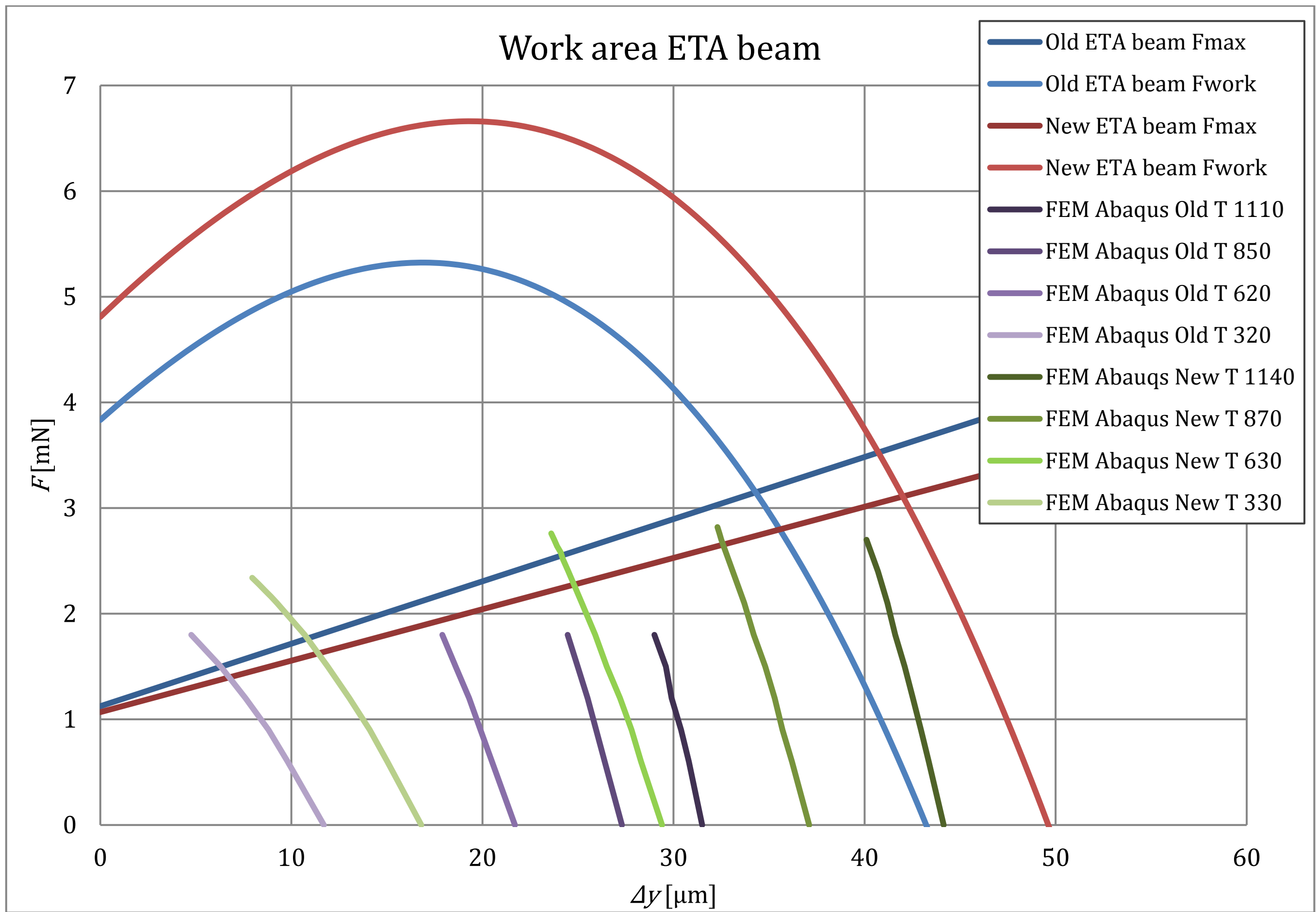

Figure 20: Analytical and FEM results for the ETA beam optimization process.

The analytical model is plotted for the old and new ETA beam design. The area bordered by the x-axis, y-axis, F_{max} line and F_{work} line is the operation area of the ETA beam. The F_{max} lines are calculated for a mean temperature of T = 800 K, corresponding to a maximum temperature of T= 1100 K, using the Maloney electro-thermal numerical model **[2]**. The Young's Modulus was chosen E= 150 GPa.

The FEM simulation shows less deflection and force for the assumed maximal temperature of around T= 1100 K then the analytical model. This is as expected because the bending stress is neglected in the analytical model and thus the result is optimistic. Furthermore the bending strain influence for the old design is larger (amount of interconnections, p = 73) and this explains the larger difference between analytical model and FEM simulation compared to the new design (amount of interconnections, p = 6).

A heat sink is applied in the middle of the ETA beam for regulation of the longitudinal temperature profile in the beam. The heat sink reduces heat in the centre of the beam, where stress is highest during deflection. This increases maximum deflection for the material strength decreases near the melting point (silicon T= 1600 K). See Figure 19 for the temperature profile simulated using FEM.

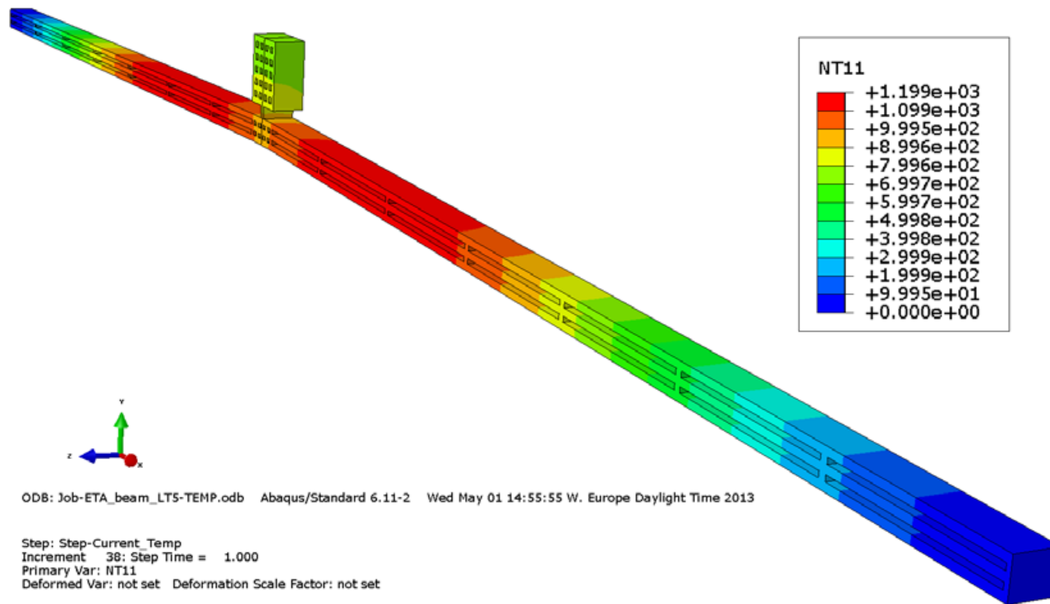

Figure 21: New ETA beam FEM Abaqus temperature profile.

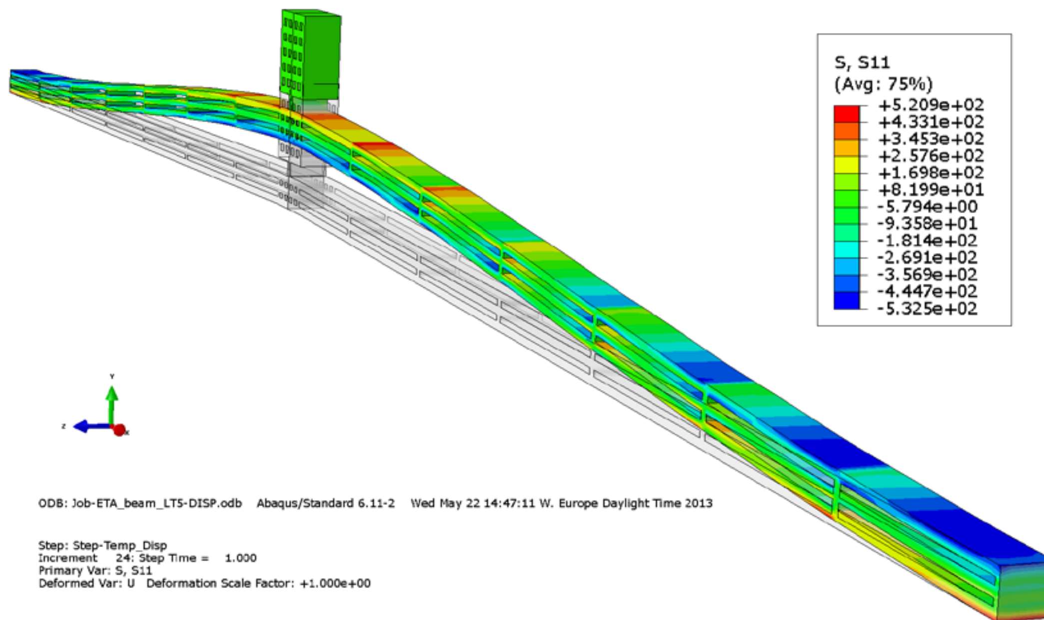

Figure 22: New ETA beam FEM Abaqus deformed stress profile, tip deflection δ = 45 µm.

Finally a second ETA beam is added in series in case the beam exerts less maximum force than calculated. A second beam doubles maximum force, but doesn't increase maximum deflection. This is why the new design ETA beam is more optimized for deflection instead of force.

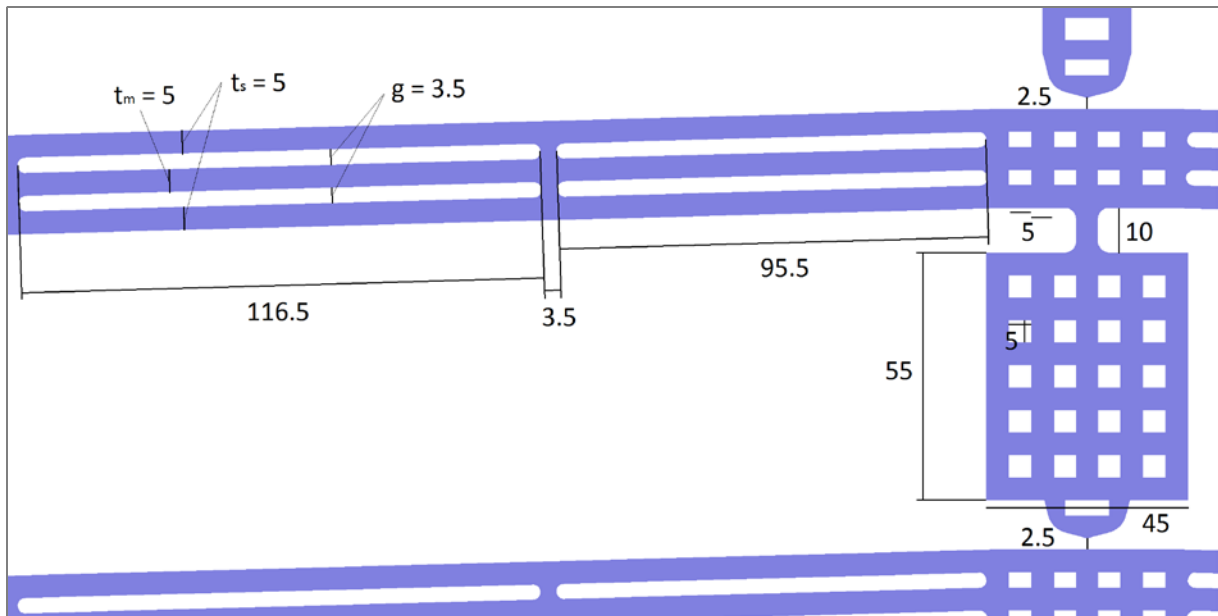

Figure 23: Final new ETA beam design outtake with dimensions (units µm). CleWin 5.0 Layout Editor.

Prevention of etching errors

As mentioned before the etching errors (etchings trenches) observed, arise from the etching process in which the outer device layer area is given a potential. This error is mostly solved by isolating all structures from the outer device layer area. In the new design the Qout connection is situated on an isolated bonding pad for all versions.

References

[1] SEM findings, Nikhef internal report, (23-01-2013)

[2] Maloney, J.M., DeVoe, D.L., Schreiber, D.S., *Analysis and design of electrothermal actuators fabricated from single crystal silicon*, University of Maryland, (2000)

[3] Enikov, E.T., Kedar, S.S., Lazarov, K.V., *Analytical and experimental analysis of folded beam and V-shaped thermal microactuators*, University of Arizona, (200X)

[4] Milligan, Donald J., Homeijer, Brian D., Walmsley, Robert G., *An ultra-low noise MEMS accelerometer for seismic imaging*, Hewlett-Packard Company, (2012)